DESIGN AND PERFORMANCE EVALUATION OF STM32-BASED MULTI-PARAMETER ONLINE MONITORING SYSTEM FOR AGRICULTURAL WATER ENVIRONMENT

/

基于 STM32 的智能水质多参数在线检测系统设计与试验

Guoyang LIU[1,2], Xiuwu PENG[1,2], Kaixuan WANG*[1,2], Zhaowen DENG[1,2], Jiayuan GONG[1,2], Bangshuai LI[1,2]

[1)] School of Intelligent Connected Vehicle, Hubei University of Automotive Technology, Shiyan 442002 / China

[2)] Hubei Engineering Research Center for Intelligent Connected Vehicles and Electronic Control, Shiyan 442002 / China

Tel: +86 18707280876; E-mail: wkx@huat.edu.cn

DOI: https://doi.org/10.35633/inmateh-78-69

Keywords: *water quality detection; turbidity sensor; pH sensor; temperature sensor; microcontroller; wireless communication*

ABSTRACT

To address the limitations of traditional water quality detection systems, such as high costs and inadequate real-time performance, a multi-source sensor collaborative monitoring solution tailored for agricultural water environments is proposed in this study. Centered on an STM32F103 microcontroller, the system integrates DS18B20 temperature, infrared turbidity, and composite pH sensors, enabling real-time dynamic monitoring of parameters via a dedicated mobile application. A 24-hour continuous operation test in a static water environment demonstrates that the system can accurately and objectively capture the physical settling and thermodynamic response characteristics of water samples, while maintaining long-term stability without crashes. Operating stably at 5V, the system achieves a rapid data response and refresh cycle of ≤2s and exhibits excellent measurement accuracy: the pH error is controlled within ±0.3, the temperature error is ±0.5℃, the turbidity resolution is 1 NTU, and the overall measurement error remains within ±5%. This system provides crucial real-time data for agricultural non-point source pollution control and offers significant technical value for ensuring water safety irrigation, developing smart agricultural water management, assessing pollution status, and formulating effective pollution mitigation strategies.

摘要

为了解决传统水质检测系统的局限性，如高成本和实时性能不足，本研究提出了一种专为农业水环境量身定制的多源传感器协同监测解决方案。该系统以 STM32F103 微控制器为中心，集成了 DS18B20 温度、红外浊度和复合 pH 传感器，可通过专用移动应用程序实时动态监测参数。在静水环境中进行的 24 小时连续运行测试表明，该系统可以准确客观地捕捉水样的物理沉降和热力学响应特征，同时保持长期稳定性而不会发生碰撞。该系统在 5V 下稳定运行，实现了快速的数据响应和≤2s 的刷新周期，并表现出优异的测量精度：pH 误差控制在±0.3 以内，温度误差为±0.5℃，浊度分辨率为 1NTU，整体测量误差保持在±5%以内。该系统为农业非点源污染控制提供了关键的实时数据，为确保水安全灌溉、发展智能农业水管理、评估污染状况和制定有效的污染缓解策略提供了重要的技术价值。

INTRODUCTION

With the advancement of agricultural intensification and large-scale operations, the extensive use of fertilizers and pesticides, along with the discharge of waste from livestock and poultry farming, has exacerbated the issue of agricultural non-point source pollution, making it increasingly prominent. Consequently, the monitoring and management of agricultural water quality, encompassing irrigation and aquaculture water, have become critically important (*Cristóvão et al., 2026; Wang et al., 2024*). Water quality detection technologies enable the timely assessment of water body contamination, thereby providing a scientific basis for the rational utilization of water resources and the effective control of agricultural non-point source pollution (*Huang et al., 2025; Liu et al., 2025*).

Guoyang Liu, Ph.D.; Xiuwu Peng, Mr.; Kaixuan Wang, master degree.; Zhaowen Deng, Prof.; Jiayuan Gong, Assoc. Prof.; Bangshuai Li, Ph.D.

Water quality monitoring is a critical component for ensuring the security and sustainable utilization of water resources. Its technological development encompasses a range of methods, from traditional chemical analysis to modern intelligent detection, including sensor technology, spectroscopic and biosensing technologies, and the Internet of Things (IoT) with intelligent monitoring systems (*Prakash et al., 2025; Morchid et al., 2025; Ahmed et al., 2025; Jabbar et al., 2024*). In recent years, researchers have focused on developing more flexible and widely applicable water quality assessment systems, such as the novel Chemical Water Quality Index (CWQI). By simplifying mathematical models and optimizing weight allocation, this index significantly enhances the accuracy and reproducibility of evaluation results (*Chemeri et al., 2023*). Simultaneously, significant breakthroughs have been achieved in portable, low-cost on-site detection technologies. For instance, colorimetric methods utilizing paper-based analytical devices (PADs) integrated with smartphones can simultaneously detect key parameters such as total hardness, chloride, nitrate, nitrite, and fluoride (*Dawan et al., 2026*). By integrating spectroscopy, computer vision, and deep learning, researchers have achieved precise assessments of pH, turbidity, and storage time for specific water bodies like tender coconut water. Data fusion strategies have further enhanced the model's discriminative accuracy to over 92% (*Wang et al., 2026*). Moreover, the monitoring of microbiological quality in irrigation water has garnered significant attention. Systematic reviews of international guidelines and testing strategies have emphasized the need for prioritized monitoring of foodborne pathogens (*Alegbeleye et al., 2023*). Luque-Söllheim et al utilized an Unmanned Aerial Vehicle (UAV) equipped with a high-resolution hyperspectral system, combined with a Radiative Transfer Model (RTM), to perform rapid remote sensing retrieval of key water quality parameters (*Luque-Söllheim et al., 2026*). Similarly, Shatnawi et al combined multispectral imagery acquired by a UAV with various artificial intelligence models to assess lake water quality. Subsequently, they trained and compared various models, including Support Vector Machine (SVM), Random Forest (RF), and Artificial Neural Network (ANN), for the high-precision prediction of water quality parameters (*Shatnawi et al., 2025*).

International researchers have proposed various STM32-based water quality monitoring methods and devices. Alam et al. developed a multi-parameter water quality monitoring system that integrates a low-cost electrochemical sensor array, custom circuitry, and a smartphone application, enabling convenient, real-time, on-site detection of parameters such as pH, residual chlorine, temperature, and BPA (*Alam et al., 2021*). Vecchio et al. designed and implemented a low-cost, flexible, and intelligent system for monitoring suspended sediment concentration, used for the fine-scale modeling of spatially heterogeneous phenomena (*Vecchio et al., 2024*). Silva et al. designed an automated, low-cost monitoring station featuring a unique flushing mechanism to prevent sensor biofouling, thereby enabling long-term, unattended monitoring of water level and turbidity (*Silva et al., 2024*). Therefore, the development of embedded water quality monitoring systems that are low-cost, highly integrated, and equipped with real-time data transmission and intelligent analysis capabilities has become a key research direction in this field. However, how to achieve the precise coordination of multi-source sensors, optimize signal acquisition and processing circuits, and ensure system stability and low power consumption in complex environments remains a critical technical bottleneck in constructing efficient and reliable monitoring terminals (*Sahu et al., 2025; Meshram et al., 2025; Lyons et al., 2023*). To address these challenges, this study aims to achieve real-time, precise, and intelligent monitoring of water quality parameters and proposes and designs a multi-source sensor collaborative monitoring scheme based on the STM32F103 microcontroller. By constructing a four-layer hardware architecture that integrates sensor acquisition, signal processing, human-computer interaction, and wireless communication, and incorporating various sensors such as those for temperature, turbidity, and pH. The fast response, stable, cost-effective, and easy to deploy embedded water quality detection system developed by our research institute can provide strong technical support for water environment management.

MATERIALS AND METHODS

System overall architecture

Centered on the STM32F103 microcontroller, the system integrates a pH/turbidity module for high-precision AD conversion, an OLED display and matrix keypad for real-time interaction and threshold configuration, and TDS and DS18B20 sensors for conductivity and temperature measurements. Supported by a stable 5V power supply, it utilizes an ESP8266 Wi-Fi module for wireless data transmission to mobile terminals. This creates an integrated “sensing-processing-interaction-transmission” hardware architecture, as shown in Fig. 1.

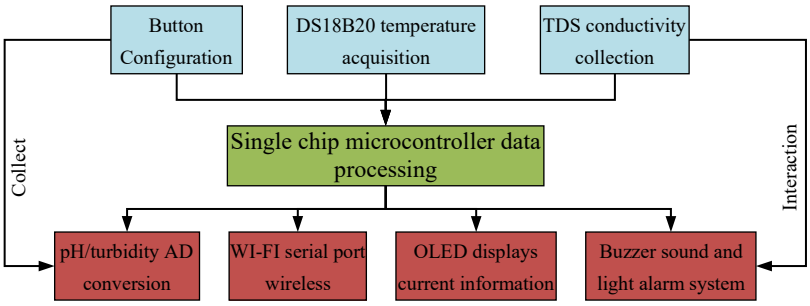

Fig. 1 - Schematic diagram of the detection system structure

Working principle

As shown in Fig. 2, the system operates on a multi-parameter monitoring architecture centered on the STM32F103 microcontroller. It integrates a DS18B20 temperature sensor, high-precision pH module, infrared turbidity probe, and TDS conductivity unit to simultaneously measure TDS, temperature, pH, and turbidity. Data is acquired via bus protocols and ADC conversion to ensure accuracy. The drive circuit consists of P1 (a relay) and U32 (a driver chip). The relay P1 is used to control high - current loads, and the driver chip U32 provides the necessary current amplification to drive the relay, ensuring stable operation of the load control. The hardware design is also optimized by adding a 1000μF/6.3V electrolytic capacitor in parallel between the VCC and GND pins of the ESP8266 module. This capacitor effectively suppresses instantaneous current fluctuations generated during Wi-Fi communication, stabilizes the power supply voltage, and prevents potential module resets or connection interruptions caused by voltage drops. An OLED display and matrix keypad facilitate real-time visualization and alarm threshold configuration, triggering audible and visual alarms when limits are exceeded. Powered via USB, the system uses an ESP8266 Wi-Fi module to upload data to a mobile app for remote monitoring. The software, developed in Keil using modular programming, implements a dynamic threshold comparison mechanism for intelligent alarm triggering.

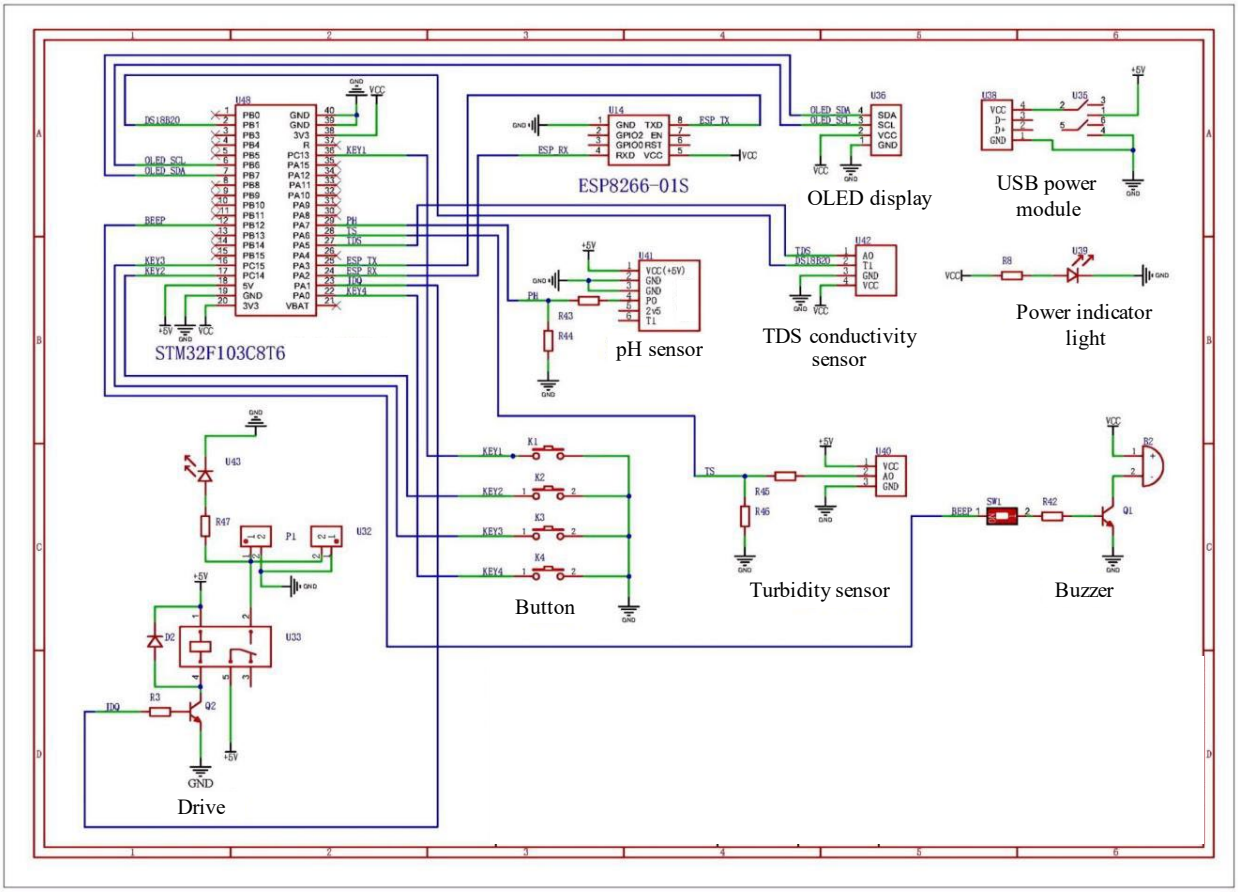

Fig. 2 - Overall electronic schematic of the detection system

System hardware design

Key control circuit and power supply circuit

A parallel four-microswitch architecture is employed for the user interface, where each switch connects one terminal to two I/O ports of the microcontroller and the other terminal to ground. In the untriggered state, the I/O ports maintain a high-level output; when a key is pressed, the I/O port transitions from high to low through the grounding path, sending a low-level trigger signal to the microcontroller. Due to contact bounce during mechanical switching, the keyboard detection mechanism incorporates a debounce algorithm module to ensure accurate key value recognition and reliable signal detection. This module determines valid key signals by monitoring the level status in real time and applying software filtering.

The system is driven by a 5V DC power supply, a voltage level selected for its compatibility with the logic levels of the microcontroller and the operating requirements of the peripheral sensors and OLED display, ensuring stable performance with low power consumption. The power module consists of a four-pin power supply interface and a six-pin power switch. The power supply interface is designed to connect external USB power input—facilitating the use of standard adapters or portable power banks—with the fourth pin serving as the ground terminal. The power switch controls the overall power supply to the microcontroller unit, with its first and third pins being functionally symmetric to the fourth and sixth pins, both serving as positive power output terminals.

Alarm circuit and OLED display

The alarm mechanism is triggered when abnormal conditions are detected, such as temperature falling below the preset threshold, pH value deviating from the safe range, or absence of water in the container. The buzzer driving circuit adopts an NPN bipolar jun0000ction transistor (BJT) driving topology: the transistor base is connected to the microcontroller's I/O port through a current-limiting resistor, the collector is linked to the positive terminal of the buzzer and the power bus, and the emitter is grounded, forming a common-emitter amplifier configuration. NPN bipolar junction is a three-terminal semiconductor device consisting of two N-type regions separated by a P-type region, acting as a current-controlled switch in the circuit.

The OLED display module circuit utilizes a P5 four-pin header interface to connect with the display. Signal transmission is achieved by connecting the display's SCL pin to the microcontroller's B6 pin for serial clock signal transmission, and the SDA pin to the MCU's B7 pin for serial data communication. In the circuit structure of the OLED display module, the P5 header employs a 4-pin design specifically dedicated to connecting the OLED display. Regarding signal transmission, the SCL pin of the display is connected to pin B6 of the microcontroller unit (MCU), which is responsible for transmitting the serial clock signal. Additionally, the SDA pin is connected to pin B7 of the MCU, enabling serial data communication via this interface.

Based on the SSD1306 vertical address increment architecture, the system uses a big-endian byte data organization method. Display data is implemented through layered driving: the underlying hardware abstraction layer configures registers via I2C/SPI protocols, while the application layer optimizes data compression rates through bit manipulation algorithms, writing data batches to GDDRAM via DMA channels. A partial update strategy reloads data for changed regions, combined with a gamma correction algorithm to enhance display stability.

Temperature sensor and turbidity acquisition module

The DS18B20 digital temperature sensor is employed as the core temperature measurement element, communicating via the single-bus protocol. This sensor is factory-calibrated, and a high measurement accuracy of ±0.5°C across the operating range of -10°C to 85°C is guaranteed, with an even tighter error margin of ±0.2°C within the 0–50°C range. Regarding the working principle, a conversion sequence is initiated by the STM32 microcontroller through the transmission of a start signal via an I/O port. A 40-bit data frame is output by the sensor in response, with the most significant bit (MSB) transmitted first. To ensure data integrity, the received data—comprising temperature integer values—are verified by the microcontroller using a 4-byte data packet and an 8-bit cyclic redundancy check (CRC). The validated temperature readings are then displayed in real time on the OLED screen.

The structural schematic of the sensor is illustrated in Fig. 3. The optical transmission principle is adopted by the infrared turbidity sensor. Its core structure is composed of an infrared emitter and a photoreceiver. During operation, the water sample is penetrated by infrared light beams generated by the emitter, and the transmitted light intensity is converted into a corresponding electrical signal by the receiver. Physically, scattering and absorption of the incident light are induced by suspended particles in the water, resulting in a regular attenuation of transmitted light intensity as turbidity increases.

Leveraging the positive correlation between suspended solids concentration and turbidity, as well as the negative correlation between light transmittance and turbidity, quantitative detection of water turbidity is achieved by real-time monitoring of the output current signal from the receiver.

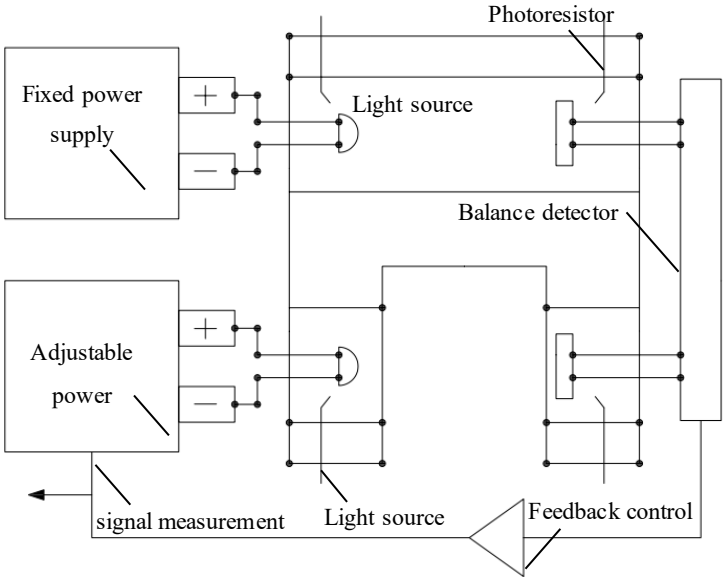

Fig. 3 - Schematic diagram of the turbidity sensor structure

Based on optical theory analysis, when a parallel beam of light is incident perpendicularly from air into the water body to be measured, the light intensity at an underwater depth of Y can be expressed by the following mathematical equation:

$$I_Y = \mathrm{K}_0 I_0 e^{-K_1 TY} \tag{1}$$

From Equation (1), it can be seen that there is a quantitative relationship between the incident light intensity I_0 and the water turbidity T. Where K_0 represents the transmission characteristics of parallel light at zero incident angle, and K_1 reflects the absorption characteristics of the solution to parallel light. When the particle size distribution in the water body is uniform, the scattered light intensity dI_{S1} in a specific direction is positively correlated with turbidity, which microscopically manifests as the variation of scattered light intensity in the dy region being proportional to the turbidity parameter.

$$dI_{S1} = K_2 T I_Y dy \tag{2}$$

where K_2 is the scattering coefficient of the solution for light, and I_Y is the light intensity at depth Y. Substituting Equation (1) into Equation (2) yields the scattered light along the X direction at depth Y as:

$$dI_{S1} = K_2 T K_0 I_0 e^{(-K_1 TY)} dy \tag{3}$$

The actual intensity of the scattered light that arrives is:

$$dI_S = dI_{S1} e^{-K_1 TX} \tag{4}$$

In the optical scattering model system, the variable X represents the spatial distance that scattered light travels to reach the surface of the silicon photocell. Based on the aforementioned physical definitions, it can be derived that along the X-axis direction, from the initial position 0 to the critical value Y_0, the integral expression for the scattered light intensity is:

$$\mathrm{I_S} = \int_0^{Y_0} dI_S = \int_0^{Y_0} e^{-K_1 TX} dI_{S1} = \int_0^{Y_0} K_0 K_2 I_0 T e^{-K_1 TY} e^{-K_1 TX} dy = \frac{K_2 K_0}{K_1} I_0 e^{-K_1 TX} (1 - e^{-K_1 TY_0}) \tag{5}$$

Expanding $e^{-K_1 TX}$ and $e^{-K_1 TY_0}$ using Taylor's formula yields the equation:

$$I_S = \frac{K_2 K_0}{K_1} I_0 (1 - K_1 TX + \frac{K_1 TX}{2!})(K_1 Y_0 T - \frac{K_1 Y_0 T}{2!}) \tag{6}$$

Under the conditions of extremely short transmission distance and small time parameter T, the value of the $K_1 T$ term is much smaller than 1, and the magnitude of its quadratic and higher-order terms is even more negligible and can be ignored.

Based on this, reasonable approximations can be made for the first-order and higher-order terms, leading to a simplified expression after mathematical derivation. When the incident light intensity I_0 is constant, the received light intensity I_s is directly proportional to the turbidity T.

In terms of light source power supply, a precision constant current drive architecture is employed with integrated soft-start circuitry to suppress inrush current during power-on. Experiments have shown that LED light intensity has a linear relationship with drive current but a nonlinear relationship with voltage (±5% voltage fluctuation can lead to ±30% light intensity deviation). Through a closed-loop control system constructed with TL431 reference source and operational amplifier feedback circuitry, the drive current fluctuation rate is controlled within ±0.5%, improving light intensity stability by 82.6% compared to traditional constant voltage schemes, significantly ensuring the consistency of light source radiation intensity during long-term operation. The dual photodetector measurement system can eliminate environmental interference through ratio operation:

$$T = a\frac{V_s}{V_R} \tag{7}$$

where V_s is the scattered light voltage, V_R is the reference light voltage, and a is the system calibration coefficient. Experimental data show that within the temperature range of -10°C to +50°C, the voltage drift caused by the temperature difference effect of the photodetector is less than 0.1mV/°C, which can be negligible. As shown in Fig. 4, the turbidity-voltage relationship model was established through the least squares method as follows:

$$y = -1120.4x^2 + 5742.3x - 4352.9 \tag{8}$$

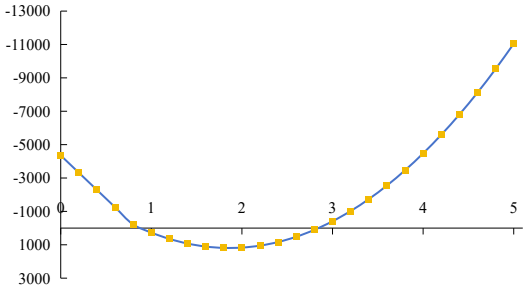

Fig. 4 - Relationship curve between turbidity and voltage

pH collection module

As shown in Fig. 5, an E-201C rechargeable composite pH sensor was selected for pH measurement. Solutions can be classified into three categories based on pH value: acidic solutions: 0≤pH<7; neutral solutions: pH=7; alkaline solutions: 7<pH≤14. For each unit decrease in pH value, the acidity of the solution increases by 10 times; conversely, an increase in pH reflects a significant increase in alkalinity.

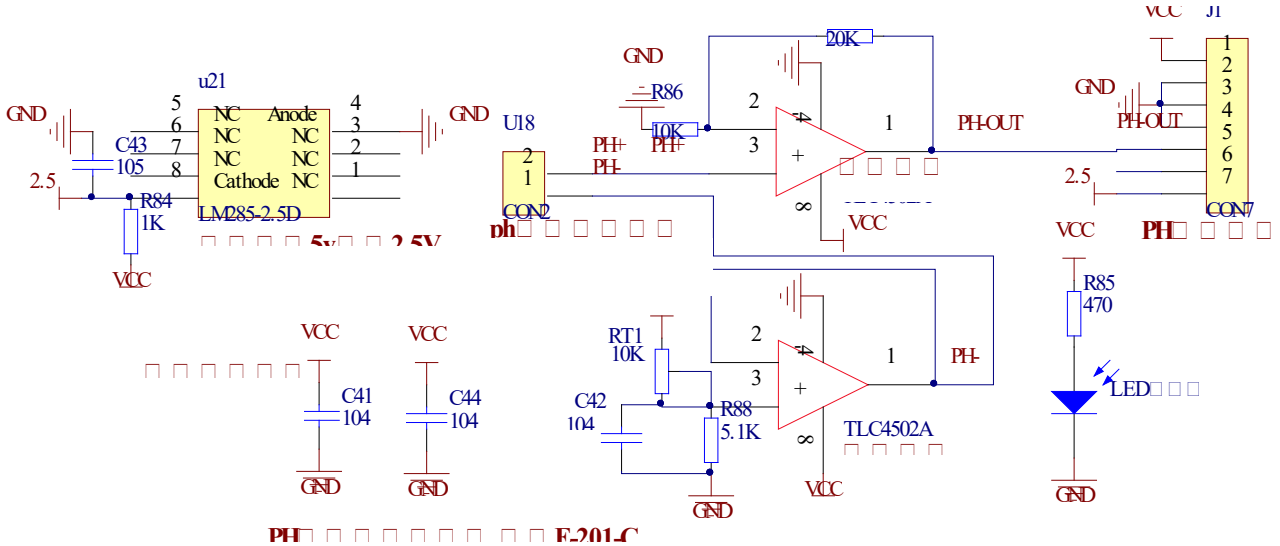

Fig. 5 - Internal circuit diagram of pH sensor

The detection system utilizes the voltage signal output by the pH sensor to perform analog-to-digital conversion through the A0 port, thereby obtaining the corresponding pH value. These three calculation formulas are shown in equation (9). By solving any two equations simultaneously, the slope parameter and intercept term characterizing the relationship between pH and voltage can be derived; accordingly, the linear mathematical model of pH and voltage in equation (10) is established as follows:

$$\begin{cases} 3.071k + b = 4 \\ 2.535k + b = 7 \\ 2.066k + b = 10 \end{cases} \quad (9)$$

$$y = -5.9647x + 22.255 \quad (10)$$

TDS conductivity measurement module and Wi-Fi transmission circuit

Total Dissolved Solids (TDS) is a key indicator characterizing the mass concentration of soluble inorganic salts in water, defined as the residue mass after filtering 1 liter of water sample through a 0.45μm filter membrane and constant temperature drying at 180°C. Its value shows a significant positive correlation with the ionic strength and conductivity of the water sample, reflecting the migration ability of free ions in the solution. The unit of TDS is usually milligrams per liter (mg/L), and it can also be expressed as ppm (parts per million). The unit of electrical conductivity is microsiemens per centimeter (μS/cm), which is a commonly used unit for electrical conductivity in water quality monitoring. The TDS value could be indirectly calculated by measuring the solution conductivity. Since the relationship between conductivity and TDS is not linear. Related research on electrolyte compatibility shows that the conversion coefficient between total dissolved solids and conductivity can be flexibly adjusted within the range of 0.3 to 1.0. The relationship between TDS and conductivity is shown in Table 1.

Table 1

Relationship between TDS and Conductivity

Conductivity (μS/cm)	TDS (ppm)	Conductivity (μS/cm)	TDS (ppm)	Conductivity (μS/cm)	TDS (ppm)
0.1	0	75	35.3	650	305.5
0.2	0.1	100	47	700	329
0.5	0.2	125	58.8	750	352.5
1	0.5	150	70.5	800	376
1.5	0.7	175	82.3	850	399.5
2	0.9	275	129.3	900	423
2.5	1.2	300	141	950	446.5
5	2.4	350	164.5	1000	470
10	4.7	400	188	1250	587.5
15	7	450	211.5	1500	705
20	9.4	500	235	1750	822.5
25	11.8	550	258.5	2000	940
50	23.5	600	282	2500	175

When the TDS detection module performs data transmission, it mainly relies on the serial communication protocol. The module only needs to establish a serial communication connection with the microcontroller to complete the data interaction function, with a communication baud rate of 9600 bps. The current TDS value can then be obtained by parsing the communication commands.

A low-power wireless communication network is constructed using a UART-WI-FI transparent transmission module based on ESP8266, which integrates the IEEE 802.11 b/g/n protocol stack and supports AP, STA, and hybrid mode networking. The module operates at 3.3V and implements parameter configuration and data transmission through serial AT command sets, with a maximum communication distance of 100m.

Compared to traditional Bluetooth/ZigBee solutions, it offers superior network coverage capability and cross-platform compatibility. Pin 4 is connected to the MCU pin PA10 to implement module status control; Pin 8 is connected to the MCU pin PA9 to facilitate data transmission and reception; and Pin 1 is grounded to ensure a consistent logic level reference.

System software design

Main program design

The system software design initiates with a comprehensive initialization process that configures external devices and internal registers, including GPIO pin assignments for the DS18B20 single-wire interface, ADC channels for turbidity and pH sensors, PWM for TDS, USART for Wi-Fi, I²C for the OLED display, and the matrix keypad. Following this setup, the system polls the reset key status; if no reset signal is detected, it proceeds to the main subroutine execution phase. During this operational cycle, the system performs multi-source data acquisition by driving the DS18B20 for temperature conversion, utilizing dual-channel ADC scanning with DMA transfer to acquire and linearly calibrate turbidity and pH analog signals, and calculating TDS conductivity via PWM frequency detection. Simultaneously, the system manages human-machine interaction by refreshing the OLED screen with real-time sensor data and network status, scanning the keypad for threshold adjustments which are stored in EEPROM, and conducting safety monitoring where data limit violations trigger local audible and visual alarms alongside JSON-formatted alert transmissions to the cloud via Wi-Fi. The overall logic of this main program is illustrated in the flowchart presented in Fig. 6.

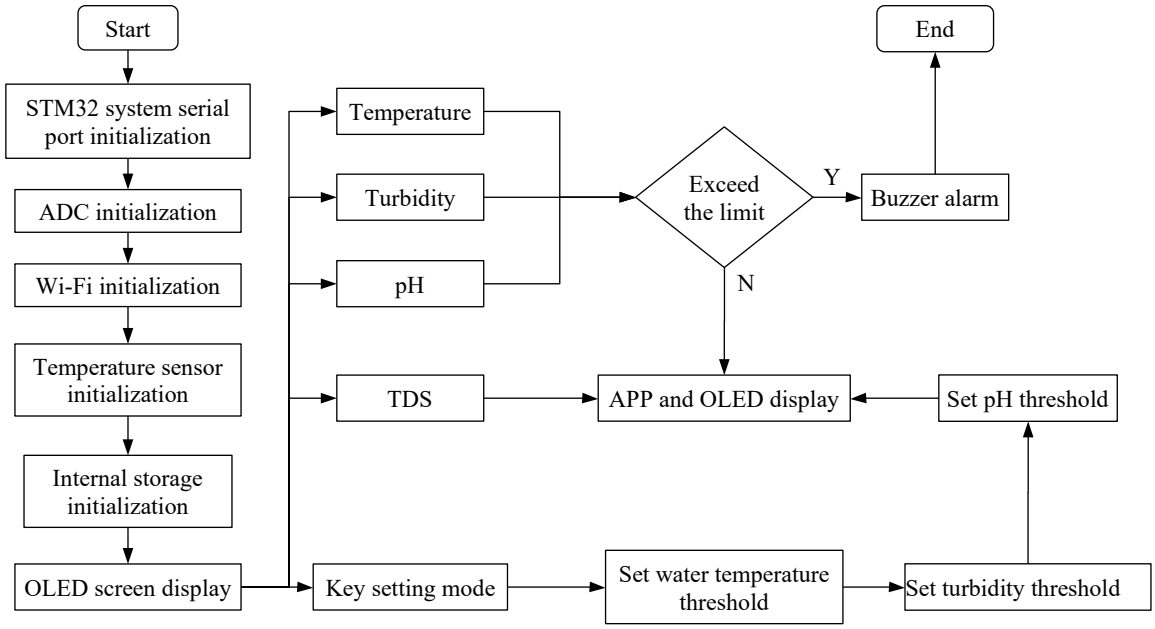

Fig. 6 - Flowchart of the main program of the system

Display screen and temperature acquisition program design

The OLED display module adopts a status detection mechanism to ensure the module is ready before sequentially executing instruction control word writing and display data transmission. The STM32 completes register address setting and data writing by configuring open-drain mode IIC pins, achieving data visualization control. The DS18B20 temperature sensor strictly follows the single-bus protocol timing specifications (reset hold 480–750μs, response detection 60–240μs), and through I/O initialization, sensor reset, response detection, data reading, and algorithm conversion processes, stores temperature data to the microcontroller memory unit. The system constructs a complete temperature monitoring architecture through the coordinated operation of precisely controlling the OLED display process (instruction/data transmission status detection, IIC communication timing) and DS18B20 acquisition process (bus idle high-level maintenance, reset pulse width control, response signal detection), ensuring real-time data acquisition (μS-level response) and display control reliability (state machine driven), ultimately achieving accurate environmental temperature monitoring and visual presentation.

The specific flowchart is shown in Fig. 7.

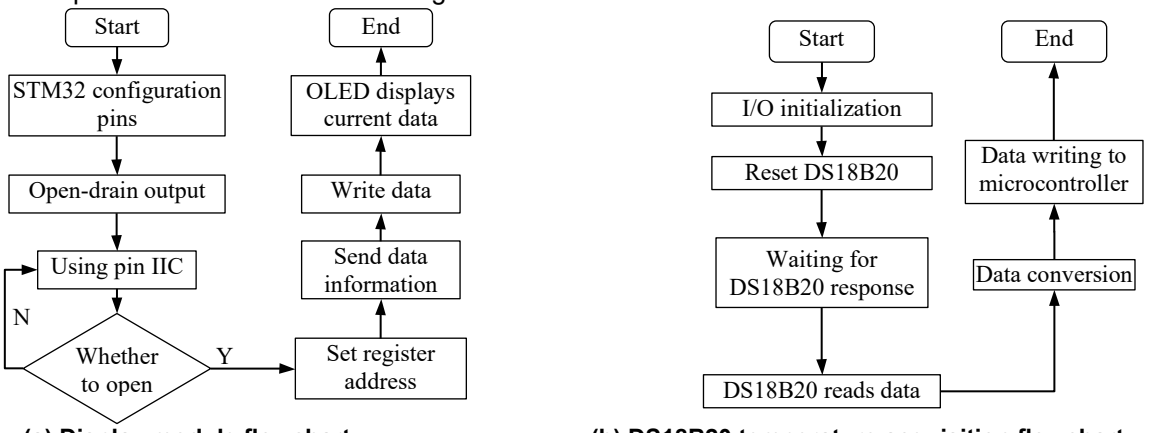

Fig. 7 - Flowchart of the main program of the system

Human-machine interaction and data acquisition program design

The human-machine interaction module adopts a four-pin matrix keypad with 10ms polling and a state machine debounce algorithm for threshold configuration, storing parameters in on-chip Flash. The alarm circuit, based on an NPN driving topology, complies with IEC 60730 safety standards, triggering audible and visual alarms when monitored parameters exceed limits. For data acquisition, pH and turbidity signals are processed via the built-in dual-channel ADC, while TDS acquisition utilizes a serial communication protocol with frame synchronization and parity checks to ensure transmission reliability. The system program flow is illustrated in Fig. 8.

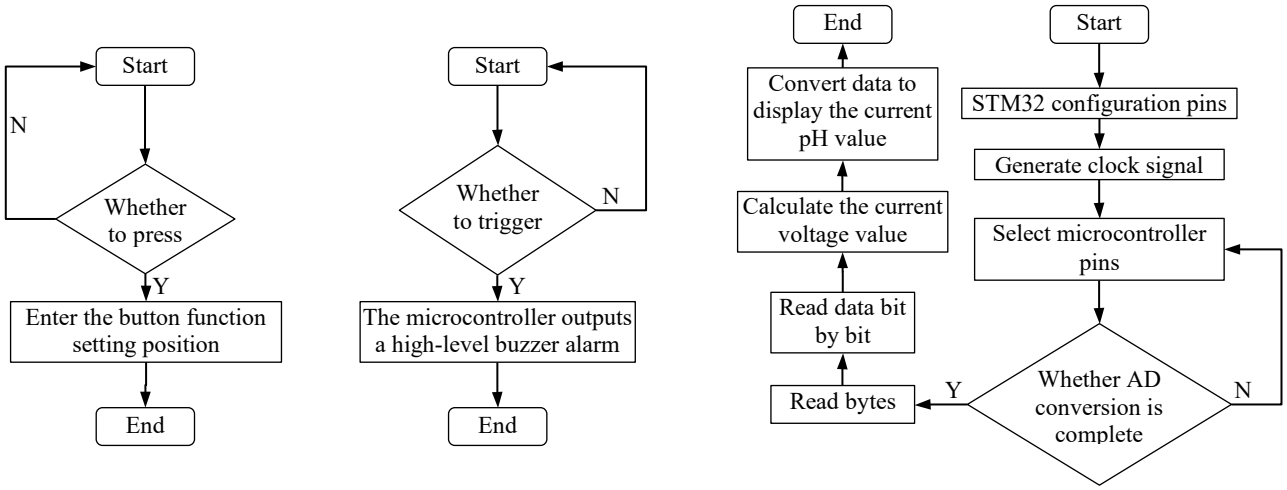

Fig. 8 - Flowchart of the main program of the system

TDS acquisition and Wi-Fi wireless communication program design

The TDS serial communication protocol requires configuring frame synchronization, data structure, parity checks, and stop bits, ensuring strict baud rate matching. As shown in Fig. 9, the acquisition process sequentially executes ADC initialization, channel selection, and bit-by-bit frame parsing to calculate real-time TDS values. The ESP8266 module utilizes AT commands to establish a Wi-Fi hotspot connection. The communication flow initializes the serial port, configures AP mode parameters, and monitors transmission status to enable wireless data transfer to the mobile terminal.

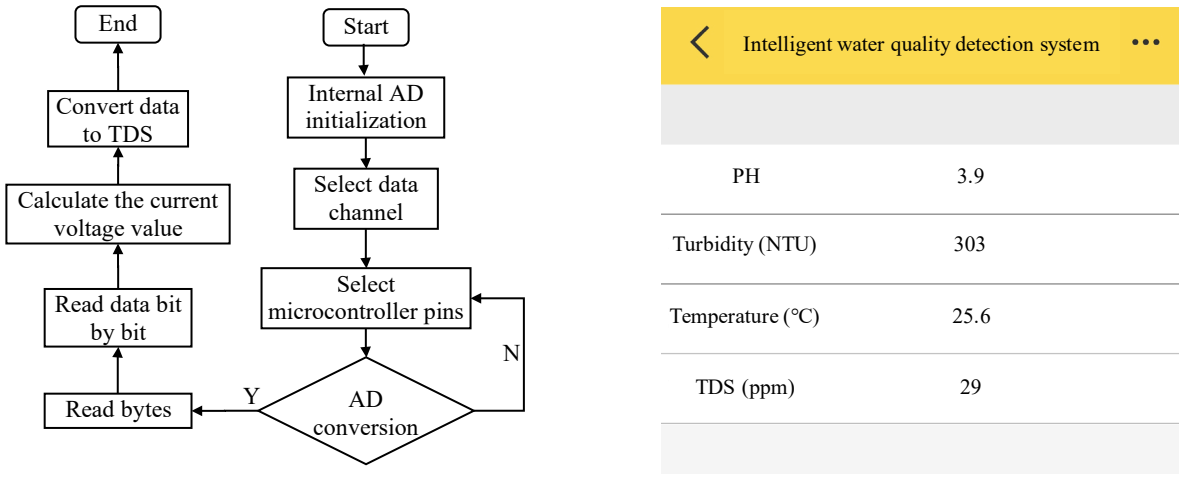

(a) Display module flowchart **(b) Mobile software interface**

Fig. 9 - TDS program design flowchart and mobile software interface

RESULTS

Experimental setup

The sensor network was initialized, and the Wi-Fi module was set to Access Point (AP) mode. Upon system power-up, the OLED's real-time display of water temperature, pH value, turbidity, and TDS data was verified. The buzzer's threshold alarm response speed and mobile data synchronization functionality were tested. Results indicate stable system operation under a 5 V power supply, with a data refresh cycle of ≤2s. To handle signal noise during acquisition, a simple RC low-pass filter was added right before the ADC input. This resistor-capacitor combination naturally blocks high-frequency interference while letting the actual low-frequency water quality signals pass smoothly into the ADC. Thanks to this filtering step, the TDS measurement fluctuation was successfully brought down and controlled within ±5%, meeting multi-scenario water quality monitoring requirements.

Experimental testing

In the laboratory, as depicted in Fig. 10, a simulation of a typical agricultural water environment was created. This involved preparing various water quality samples, including standard buffer solutions with known pH levels, suspensions with varying turbidity, and solutions with different total dissolved solids (TDS) values. The assembled water quality detection system was then connected to a 5V DC power source and initialized upon powering up. The OLED display was monitored to ensure it correctly showed system startup information, including initial readings for each parameter. Subsequently, the pH composite electrode, infrared turbidity sensor, DS18B20 temperature probe, and TDS conductivity module were sequentially immersed in various water quality samples. The data collection feature was activated, and the system's readings, updated every second, were recorded. The alarm thresholds for each parameter were adjusted using the key setting function to confirm that the system could trigger acoustic and optical alarms when parameters exceeded their limits. The functionality of the buzzer and LED alarm lamp was also verified. The Wi-Fi module was activated, and a mobile application was connected to the hotspot established by the system to check if real-time water quality data could be received and displayed on the mobile device. The system was operated continuously for 24 hours to record any fluctuations during data collection and to check for any anomalies or system crashes, thereby confirming the system's long-term operational stability.

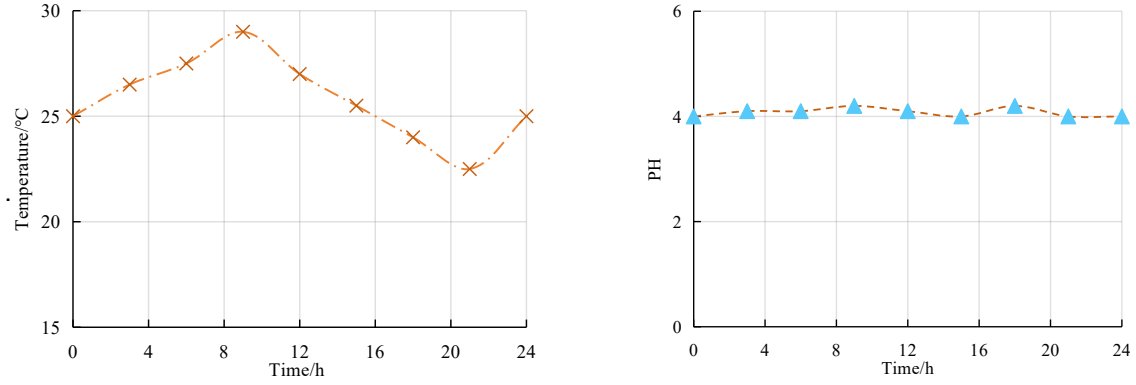

(a) Test results of temperature variation over time **(b) Test results of pH variation over time**

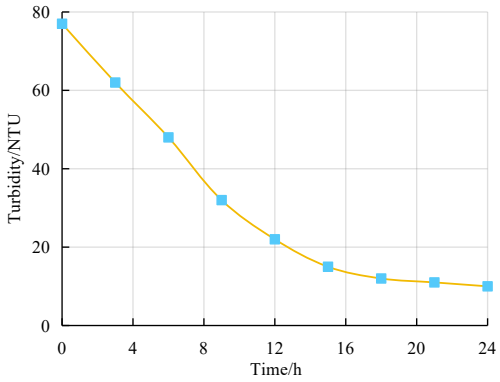

(c) Test results of turbidity variation over time

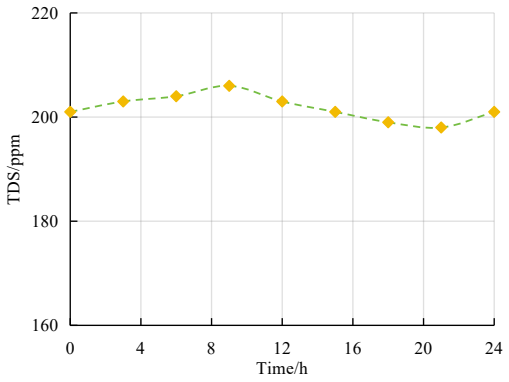

(d) Test results of TDS variation over time

Fig. 10 - Water quality testing experiment of the detection system

The monitoring results show that in a static beaker environment, the water quality parameters exhibited distinctly different variation patterns over the 24-hour period, yet these patterns mutually corroborated each other. The temperature curve was highly synchronized with the laboratory room temperature, displaying a typical single-peak profile. It reached a peak of 29°C at the 9th hour and dropped to a trough of 22.5°C at the 21st hour, reflecting the physical characteristic of a small water volume having low heat capacity and responding rapidly to ambient temperature changes. Meanwhile, turbidity exhibited a clear exponential decay trend, steadily dropping from an initial 77 NTU and eventually stabilizing at 10 NTU. The decline gradient was noticeably steeper during the first 9 hours (from 77 down to 32 NTU) than in the remaining 15 hours, which perfectly aligns with the physical law of natural gravity settling of suspended particles in a static, undisturbed water body. Throughout the monitoring cycle, the pH value demonstrated exceptional chemical stability, fluctuating only within an extremely narrow range of 4.0 to 4.2. This minimal ±0.2 variation falls well within the normal measurement accuracy of the sensor, indicating that under the strongly acidic condition of pH 4.0, the water body was completely immune to interference from atmospheric carbon dioxide dissolution equilibria. Without the driving force of biological photosynthesis or respiration, the acid-base system essentially remained locked. Furthermore, the TDS data showed a remarkably strong positive correlation with the temperature curve; its peak (206 ppm) and trough (198 ppm) readings corresponded precisely to the temperature highs and lows. Consequently, the apparent changes in the readings were purely the result of physical fluctuations in ionic activity and electrical conductivity caused by water temperature shifts, while the actual mass of total dissolved solids in the water sample remained completely unchanged. Beyond accurately and objectively reflecting these physical settling processes and thermodynamic responses, the overall reliability of the system was further substantiated by its technical performance metrics. Test results indicated that the system maintained a measurement error of ±0.3 for pH values across various water quality samples, a turbidity detection resolution of 1 NTU, a temperature measurement accuracy of ±0.5°C, and a TDS measurement error within ±5%. The system took no more than 2s to display stable data after sensor immersion and could trigger acoustic and optical alarms within 500 milliseconds when parameters exceeded their limits. Moreover, the mobile terminal received early warning notifications within 1s, demonstrating a rapid response capable of promptly indicating water quality changes. After 24 hours of continuous operation, the system's data collection remained stable without any anomalies or crashes, ensuring normal data refresh and alarm functionality, thereby proving its long-term operational stability. The fluctuation of pH and turbidity data remained within a ±5% range, ensuring the system's normal operation and the proper functioning of the alarm without any false or missed alerts, thereby comprehensively demonstrating the system's robustness and anti-interference capability.

CONCLUSIONS

Focusing on the demand for water quality monitoring, an intelligent multi-parameter detection system based on the STM32F103 microcontroller is designed and developed in this paper. The research work mainly encompasses hardware architecture design, software algorithm development, and system anti-interference optimization. At the hardware level, an embedded platform centered on STM32F103C8T6 is constructed, wherein pH composite electrodes, infrared turbidity sensors, DS18B20 temperature probes, and TDS conductivity modules are integrated. Synchronous acquisition and AD conversion of four types of water quality parameters are achieved through signal interface and filtering circuits.

A human-computer interaction system is formed by designing an OLED display screen, a buzzer alarm circuit, and an ESP8266 WI-FI transmission module. At the software level, data acquisition programs are written based on the Keil development environment, signal stability is enhanced using sliding average filtering algorithms, and excessive warning functions are realized by combining threshold comparison mechanisms. Based on 24-hour continuous testing verification, stable operation under a 5V power supply environment is confirmed, with a rapid data dynamic refresh cycle of ≤2s. Excellent measurement precision is demonstrated, where the pH error is controlled within ±0.3, the temperature error is ±0.5℃, and the turbidity resolution reaches 1 NTU. In addition, by introducing an RC filter circuit, electromagnetic interference has been effectively suppressed and the overall parameter fluctuations have been kept within ±5%. Ultimately, real-time monitoring capabilities, along with local sound-light alarms and mobile terminal data synchronization, are successfully realized, providing a cost-effective and highly reliable IoT solution for environmental monitoring.

ACKNOWLEDGMENTS

This study was financially supported by the Natural Science Foundation of Hubei Province (Grant No. 2025AFD232) and Doctoral Scientific Research Foundation of Hubei University of Automotive Technology (Grant No. BK202490). The authors declare no conflict of interest.

REFERENCES

[1] Ahmed N., Shakoor N. (2025). Advancing agriculture through IoT, Big Data, and AI: A review of smart technologies enabling sustainability. *Smart Agricultural Technology*, vol. 10, pp. 100848.

[2] Alam A.U., Clyne D., Deen M.J. (2021). A Low-Cost Multi-Parameter Water Quality Monitoring System. *Sensors*, vol. 21, pp. 5114.

[3] Alegbeleye O., Sant'Ana A.S. (2023). Microbiological quality of irrigation water for cultivation of fruits and vegetables: An overview of available guidelines, water testing strategies and some factors that influence compliance. *Environmental Research*, vol. 220, pp. 114771.

[4] Chemeri L., Cabassi J., Taussi M., Venturi S. (2023). Development and testing of a new flexible, easily and widely applicable chemical water quality index (CWQI). *Journal of Environmental Managemen*t, vol. 348, pp. 119383.

[5] Cristóvão M., Sério J., Marques A., Bento-Silva A., Gossard M., Vergara-Diaz O., Silva A.F., Nunes M., Bronze M.R., Brás de Oliveira P., Barreto Crespo M.T., Goulão Crespo J., Jorge Pereira V. (2026). Treatment of wastewater effluents using nanofiltration and low pressure UV photolysis to produce high quality water for food production. *Water Research*, vol. 289, pp. 124782.

[6] Dawan P., Chaiyasith W.C., Sawangmek S. (2026). Development of a paper-based analytical device integrated with a custom-built smartphone application for on-site colorimetric water quality testing. *Talanta*, vol. 298, pp. 128957.

[7] Huang X., Xiong J., Lin H., Pan Z., Wang K., Zhang M., Zhu Z., Ou Y. (2025). Research on water quality detection integrating spectral analysis and automated control. *Spectrochimica Acta Part A: Molecular and Biomolecular Spectroscopy*, vol. 339, pp. 126260.

[8] Jabbar W.A., Ting T.M., Hamidun M.F.I., Kamarudin A.H.C., Wu W., Sultan J., Alsewari A.A., Ali M.A.H. (2024). Development of LoRaWAN-based IoT system for water quality monitoring in rural areas. *Expert Systems with Applications*, vol. 242, pp. 122862.

[9] Liu S., Wang Z. (2025). Real-time effluent water quality prediction model based on BiLSTM and KAN for wastewater treatment plants. *Journal of Water Process Engineering*, vol. 78, pp. 108750.

[10] Luque-Söllheim A.L., Martín J., Medina A., Carrasco-Acosta M., García-Jiménez P., Ferrer N., Bergasa O. (2026). Hyperspectral rapid detection of bacterial content and water quality parameters in coastal bathing waters. *Marine Pollution Bulletin*, vol. 222, pp. 118705.

[11] Lyons K.J., Ikonen J., Hokajärvi A.M., Räsänen T., Pitkänen T., Kauppinen A., Kujala K., Rossi P.M., Miettinen I.T. (2023). Monitoring groundwater quality with real-time data, stable water isotopes, and microbial community analysis: A comparison with conventional methods. *Science of The Total Environment*, vol. 864, pp. 161199.

[12] Meshram S., Ramachandran S., Mangal A., Shahu S.K.M., Elampulakkadu A., Mukhopadhyay A., Rao P.K., Pillai S.R.B., Baghini M.S., Bandyopadhyaya R. (2025). AquaSys: An autonomous, wireless real-time water quality monitoring system for pH and temperature measurement. *Sensors and Actuators A: Physical*, vol. 396, pp. 117107.

[13] Morchid A., Alblushi I., Khalid H.M., Qjidaa H., El Alami R. (2025). Integrating IoT and fuzzy logic for intelligent irrigation in sustainable agriculture for improving water scarcity: Benefits and challenges. *Sustainable Computing: Informatics and Systems*, vol. 48, pp. 101191.
[14] Prakash S., Jena K., Mishra A.K. (2025). Bimetallic complexation for significant fluorescence enhancement of faecal pigment towards water quality testing. *Journal of Photochemistry and Photobiology A: Chemistry*, vol. 459, pp. 116041.
[15] Sahu N., Maldhure A. (2025). Framework for evaluating the performance of water quality sensors. *Cleaner Water*, vol. 4, pp. 100144.
[16] Shatnawi N., Abu-Qdais H., Abu-Dalo M., Salem E.K. (2025). Assessing water quality of a lake using combination of drone images and artificial intelligence models. *The Egyptian Journal of Remote Sensing and Space Sciences*, vol. 28, pp. 426-435.
[17] Silva P.V.R.M., James R.B., Russell K.L., Fletcher T.D., Gisi M.F.S., Navratil O., Cherqui F., Cossart E. (2024). An automated low-cost monitoring station for suspended sediments and water level. *HardwareX*, vol. 20, pp. e00594.
[18] Vecchio A., Bini M., Lazzarotti M., Luppichini M., Palmieri M. (2024). A smart, multi-configuration, and low-cost system for water turbidity monitoring. *Results in Engineering*, vol. 24, pp. 103116.
[19] Wang T., Huang R., Wei Z., Xie M., Chen L., Wang W.T., Yun Y.H. (2026). Multimodal nondestructive testing of tender coconut water quality using spectroscopy, computer vision, and deep learning. *Food Control*, vol. 180, pp. 111660.
[20] Wang Z., Li T., Liang W., Fu B., Li J., Yan J. (2024). Uncovering the structure and evolution of global virtual water and agricultural land network. *Sustainable Production and Consumption*, vol. 51, pp. 599-611.